A rigid body dynamics simulation enhanced representative volume element builder for CNT/Al composite

J. F. Zhang · X. X. Zhang · Z. Y. Liu · Q. Z. Wang · B. L. Xiao ·
Z. Y. Ma

Abstract A novel representative volume element (RVE) builder is developed to solve the strong "framing effect" problem in previous RVE builders. Taking advantage of rigid body dynamics simulation, the new RVE builder can construct RVEs of CNT/Al with high volume fractions and complex geometries of CNTs. 3D RVEs with random/aligned CNTs and three volume fractions (1.5, 3.0, and 4.5 vol.%) are constructed. Uniaxial tensile tests of these RVEs are simulated. The loading direction is parallel/perpendicular to the aligned CNTs. Based on the simulations, Young's moduli and stress–strain curves are calculated to study the load transfer strengthening mechanism of CNT/Al. Compared to the unreinforced Al, the 4.5 vol.% CNT/Al with aligned CNTs shows ∼ 28% increment in Young's modulus, while the one with random distributed CNTs only shows ∼ 11% increment. The simulation results match well with the reported experimental results.

1 Introduction

Discontinuously reinforced aluminum matrix composites (AMC) were widely used in the past decades because of their low density, high strength, and stiffness (Zhang et al. 2020a, 2019a; Xie et al. 2019; Ye et al. 2019; Ma et al. 2019). In recent years, carbon nanotube (CNT) reinforced AMC (CNT/Al) has been

J. F. Zhang · Z. Y. Liu · Q. Z. Wang ·
B. L. Xiao (✉) · Z. Y. Ma (✉)
Shi-changxu Innovation Center for Advanced Materials, Institute of Metal Research, Chinese Academy of Sciences, 72 Wenhua Road, Shenyang 110016, China
e-mail: blxiao@imr.ac.cn

Z. Y. Ma
e-mail: zyma@imr.ac.cn

J. F. Zhang
e-mail: jfzhang@imr.ac.cn

Z. Y. Liu
e-mail: zyliu@imr.ac.cn

Q. Z. Wang
e-mail: qzhwang@imr.ac.cn

X. X. Zhang
Heinz Maier-Leibnitz Zentrum (MLZ), Technische Universität München, 85747 Garching, Germany
e-mail: Xingxing.Zhang@frm2.tum.de

attracting much attention due to their excellent properties over traditional AMC (Liu et al. 2020; Azarniya et al. 2017; Zhang et al. 2020b; Xu et al. 2019). Because of the superior mechanical properties of CNTs (Young's modulus of $\sim$ 1 TPa and fracture strength of $>$ 30 GPa), a few additions of CNTs can improve the stiffness and strength of aluminum alloys significantly (Azarniya et al. 2017; Xu et al. 2019; Wang and Yuan 2020). Furthermore, compared with conventional ceramic particles reinforced AMC, CNT/Al shows better machinability (Azarniya et al. 2017).

To optimize the mechanical properties, it is crucial to thoroughly clarify the strengthening mechanisms of CNT/Al. Grain refinement, Orowan looping, thermal mismatch, and load transfer are the main strengthening mechanisms of CNT/Al (Liu et al. 2020, 2017; Chen et al. 2019). Among these mechanisms, the load transfer strengthening mechanism (LTSM) increases both the stiffness and strength of CNT/Al, while other strengthening mechanisms only increase strength (Huang et al. 2015; Liu et al. 2013). Therefore, the LTSM is one of the essential strengthening mechanisms in CNT/Al. Some experimental approaches, such as in-situ X-ray and neutron diffraction methods, have been developed and successfully applied in many materials to investigate the LTSM. However, it is challenging to study the LTSM in CNT/Al (Harjo et al. 2017; Roy et al. 2019; Zhou et al. 2018; Lam et al. 2020) because no CNT peak can be detected in the diffraction spectrum of CNT/Al (Suárez et al. 2013; Liu et al. 2012; Mokdad et al. 2016; Zhao et al. 2018).

In contrast, computational methods can efficiently explore the strengthening mechanisms quantitatively (Zhang et al. 2019b; Zhu et al. 2019; Figiel 2018; Li et al. 2017; Joshi et al. 2016). For example, Zhang et al. (Zhang et al. 2018a, 2018b) applied the finite element method (FEM) to assess the influences of interface strength and anisotropy of reinforcements on the LTSM of the SiC particles reinforced AMC. It was found that increasing the aspect ratio of SiC particles increases the load transfer efficiency. Taking advantage of FEM, the LTSM of CNTs could be revealed quantitatively. Using FEM to study CNT/Al requires representative volume elements (RVE) (Khalevitsky and Konovalov 2019; Guven and Cinar 2019; Müller et al. 2015; Redenbach et al. 2012) with realistic morphology, distribution, and proper volume fraction of CNTs.

Because the diameter of CNT is less than 20 nm in many cases, microstructure reconstruction from experimental data is very difficult to carry out, even with atom probe tomography (Kelly and Miller 2007) or atomic force microscope method (Efimov et al. 2007). Besides, the reconstructed RVEs can only reflect the structures of the materials that already exist, which makes it less significant for designing new materials. In addition, the experimental method is always time-consuming, making the constructed RVEs too small to be "representative" (Harper et al. 2012; Kanit et al. 2003).

Random sequential adsorption (RSA) scheme (Zhang et al. 2020b, 2014a, 2014b; Su et al. 2014; Pérez et al. 2018) can build the RVEs for CNT/Al. However, the RSA method faces the "framing effect" problems for building the RVEs of CNT reinforced composites, limiting the achievable volume fractions of CNTs. Figure 1 illustrates the framing effect in 2D. Because the placed CNTs cannot move during the RSA procedure, framed zones will be formed, which is not enough to place a new CNT. Although the framing effect in 3D is slighter than in 2D, it still seriously constrains the volume fraction of RVE when hundreds of CNTs in it. Therefore, the previous RSA method can only generate the RVEs with a relatively low volume fraction of CNTs.

Many collective rearrangement algorithms combine RSA (or sedimentation) methods with repositioning (or shrinking) processes (Ghossein and Lévesque 2013; Yu et al. 2008; Han et al. 2005; Gaiselmann et al. 2014; Salnikov et al. 2015), that are capable of generating large-sized RVEs with higher volume fractions of inclusions. Inspired by those methods, in this study, a new method for synthesizing
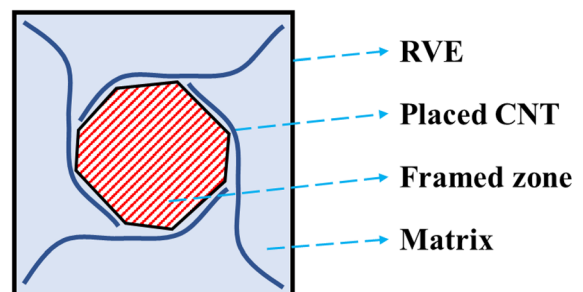

Fig. 1 Schematic diagram of "framing effect" during RSA procedure

the RVEs of CNT/Al was developed by combining RSA and rigid body dynamics simulation.

The distribution and volume fraction of CNTs can strongly affect the mechanical properties of CNT/Al. Liu et al. (2014), Zhao et al. (2017) compared the strengths of CNT/Al with random-oriented and aligned CNTs. The random-oriented CNT/Al showed lower strength than the aligned CNT/Al. The stiffness and strength of CNT/Al increased with increasing the volume fraction of CNTs (Liu et al. 2016; Wang et al. 2020a). Therefore, it is necessary to clarify the effects of alignment and volume fraction of CNTs on the LTSM in CNT/Al.

The present study aims to build the RVEs of CNT/Al with high volume fractions of CNTs. To clarify the LTSM in CNT/Al and analyze the effects of orientation and volume fraction of CNTs, three-dimensional (3D) RVE with different alignments and volume fractions of CNTs were generated. The finite element models were then set up to investigate the tensile loading behavior of CNT/Al. Young's modulus and stress–strain curves were analyzed. The stress concentration factor of CNTs was discussed.

2 Modeling procedure

2.1 Workflow of building the RVEs

A rigid body dynamics enhanced method was developed to generate large-sized RVEs with high volume fractions of CNTs. Figure 2 shows the workflow of building the RVEs of CNT/Al. In this procedure, open-source software, toolkits, and libraries were occupied. Combining those open-source tools, a software VirtualComposite-RB was developed to realize this workflow, which is divided into six steps.

2.1.1 Reinforcement generating

The first step is reinforcement generating, as shown in Fig. 2a. A CNT was created using the tube filter of software VTK (Schroeder et al. 2004). Because the CNTs in CNT/Al are not always perfectly straight (Liu et al. 2017), the longitudinal axis of the CNT was set as a spline curve. Using the spline axis also demonstrates the ability of the new method to construct complex structures of CNT. The geometry (including size and shape) can be modified by adding seed points and

adjusting their positions on the spline. Here, the nominal length and diameter of the tube were 300 and 10 nm, respectively. The shapes of CNTs in this study are identical to simplify the building procedure.

2.1.2 Loose placing

The second step is placing CNTs loosely, as shown in Fig. 2b. A box with the top open was created as a container of CNTs. A large number of CNTs were placed inside or on top of the container. The distance between CNTs should be big enough to avoid intersections with each other.

2.1.3 Rigid body dynamics simulation

The third step is rigid body dynamics simulation, as shown in Fig. 2c. The rigid body dynamics simulation was used to reduce the distance and framed zone between CNTs in Fig. 2b. Under the external force (gravity in this study), CNTs fall into the container. The equations of the rigid body motions are (Coumans 2015):

$$F = ma \tag{1}$$

$$\tau = I\omega + \omega \times I\omega \tag{2}$$

$$v_{t+\Delta t} = v_t + a\Delta t = v_t + \frac{F_{\text{ext}} + F_{\text{col}}}{m}\Delta t \tag{3}$$

$$x_{t+\Delta t} = x_t + v_{t+\Delta t}\Delta t \tag{4}$$

where m is the mass of the rigid body, x the displacement, t the time, F the resultant force on the rigid body, F_{ext} the external force, F_{col} the force caused by collision, τ the torque, I the rotational inertia, ω the angular velocity, a the accelerated velocity, v the velocity, and x the displacement. Ω is the impulse caused by collision or friction, which has a linear component and an angular component:

$$\Omega = F_{\text{col}}\Delta t = m\Delta v \tag{5}$$

$$\Omega_{\text{torque}} = \tau\Delta t = I\Delta\omega \tag{6}$$

Therefore,

$$\Delta v = \frac{\Omega}{m} \tag{7}$$
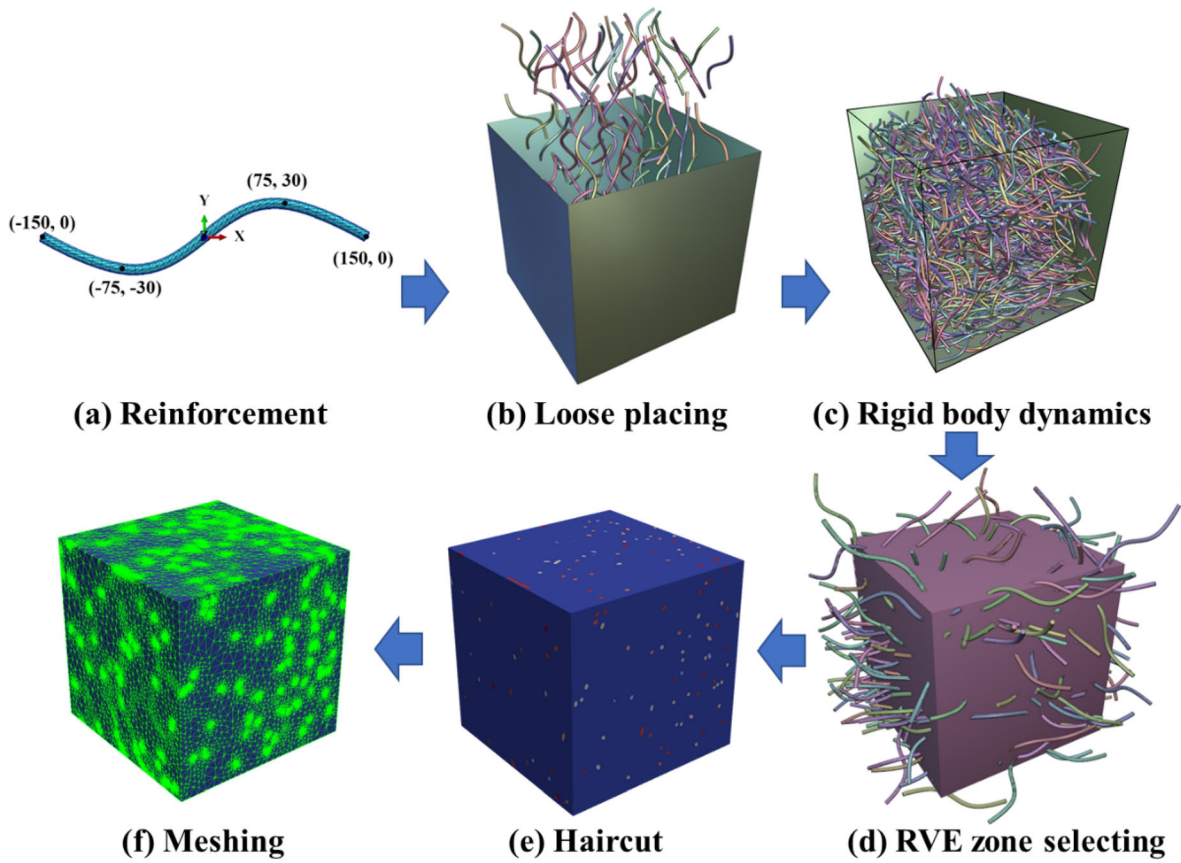
Fig. 2 Workflow of building RVEs of CNT/Al

$$\Delta\boldsymbol{\omega} = \frac{\boldsymbol{\Omega}_{\text{torque}}}{\boldsymbol{I}} = \frac{\boldsymbol{r} \times \boldsymbol{\Omega}}{\boldsymbol{I}} \tag{8}$$

where $\boldsymbol{r}$ is the relative position vector of the contact point to the center of the body mass.

When a collision involves two bodies (body A and B), the $\boldsymbol{\Omega}$ of bodies A and B can be calculated as (Coumans 2015):

$$\boldsymbol{\Omega}_{\text{A}} = -\boldsymbol{\Omega}_{\text{B}} = \frac{-(1+e)\boldsymbol{v}_{\text{AB}}\Delta\boldsymbol{n}}{\boldsymbol{n}\Delta\boldsymbol{n}\left(\frac{1}{m_{\text{A}}} + \frac{1}{m_{\text{B}}}\right) + \frac{(r_{\text{A}}\Delta n)^2}{I_{\text{A}}} + \frac{(r_{\text{B}}\Delta n)^2}{I_{\text{B}}}} \tag{9}$$

where

$$\Delta\boldsymbol{v}_{\text{AB}} = \boldsymbol{v}_{\text{AP}} - \boldsymbol{v}_{\text{BP}} \tag{10}$$

$\boldsymbol{n}$ is the normal vector for the collision (pointing toward body A by convention), e the coefficient of restitution, $\boldsymbol{v}_{\text{AP}}$ and $\boldsymbol{v}_{\text{BP}}$ the velocities of contact points on bodies A and B, respectively. The coefficient of restitution e ranges from 0 (totally plastic collision, a lump of clay landing on the floor) to 1 (totally elastic

collision or superball collision). Because the bounciness of the rigid bodies in this study increases the computational cost and massively changes the alignment of pre-placed CNTs in the second step Fig. 2b, the coefficient of restitution was set as 0.

The intersect judgement between neighboring CNTs is controlled by "geometric collision detection" of physics engine Bullet (Coumans 2015). Geometric collision detection is a large topic (Ericson 2004). For real-time physics engines nowadays, the method can be briefly stated as follows. The distance between objects at a given time needs to be calculated at first. When objects contact or intersect with each other, a collision force, $\boldsymbol{F}_{\text{col}}$ in Eq. (3), will be generated to separate the objects from each other.

By adjusting the second and third steps (loose placing and rigid body dynamics), the desired CNT orientation can be obtained. In the second step, the orientations of CNTs need to parallel to the desired orientation (or just roughly parallel to the desired

orientation). During the third step, the CNTs would rotate to lie perpendicularly to the applied gravity force after they contacted each other. When the rotations of some CNTs are greater than 30° (or less if necessary), the motions of them need to be deactivated to guarantee they do not rotate too much. Then the desired orientation of CNTs can be obtained.

The rigid body dynamics simulation was performed in software Blender (Community 2018) using the physics engine Bullet (Coumans 2015). To make the CNTs do not contact each other in the result RVE, hulls around the CNTs (convex or tube-shaped) were occupied. Using the convex hull to detect the collisions can accelerate the simulation but increase the distances between CNTs.

2.1.4 RVE zone selecting

The fourth step is RVE zone selecting, as shown in Fig. 2d. Directly using the container and all the CNTs as the RVE box can get the highest volume fraction (Sheng et al. 2019, 2016). However, this will lead to no reinforcements across the border, and it is difficult to get a target volume fraction. Therefore. in this study, the selected RVE zone is a cube in the center of the container box in Fig. 2c. Not all the CNTs would be placed in the RVE. They are selected by the following adsorption procedure.

An improved RSA method was then used to select and place CNTs inside the RVE zone, as shown in Fig. 3. Figure 3b is the original RSA method, while Fig. 3a is the improved one. Figure 3 shows that the improved method does not need to detect the intersections between CNTs, making this step much faster than the original one. During the adsorption procedure in Fig. 3a, the desired volume fraction can be controlled.

2.1.5 Haircut

The fifth step is the haircut, as shown in Fig. 2e. Because some CNTs are placed across the RVE boundaries, Fig. 2d looks hairy. To get a cubic RVE, boolean operations are applied to CNTs. The boolean operation algorithm was implemented based on the open-source library Pymesh (Zhou 2020). The structure of CNTs in Fig. 2e is also shown in Fig. 4f.

2.1.6 Meshing

The sixth step is meshing, as shown in Fig. 2f. The RVE model is meshed by software Tetgen (Si 2015) using tetrahedron elements. Figure 2e and f show the same RVE before and after meshing. The detailed effects of the mesh size are discussed in Sect. 3.2.

The new procedure is faster and more powerful than the original RSA method. For RVE with 3 vol.% CNTs, the original RSA method cost ~ 48 h while the new method only cost less than 2 h (same CPU environment). It is almost impossible for the original RSA method to generate RVEs with volume fractions above 4.0%.

2.2 Constructed RVEs

By placing random or aligned CNTs (Fig. 2b) and controlling their rotations, the RVEs with aligned CNTs (denoted by 'A') and random-oriented CNTs (denoted by 'R') were constructed. As shown in Fig. 4, six RVEs of CNT/Al were generated, i.e., six virtual composites. Three of them have aligned CNTs, and the other three have random-oriented CNTs. Three RVEs with different CNT volume fractions (1.5, 3.0, and 4.5 vol.%) were constructed by defining the target volume fractions.

The RVEs with 1.5, 3.0, and 4.5 vol.% CNTs are denoted by VF1.5, VF3.0, and VF4.5, respectively. The shape of CNTs was assumed to be curved fibers with a diameter of 10 nm and a nominal length of 300 nm. The side length of the RVEs was 600 nm and the effects of the RVE sizes are discussed in Sect. 3.2. Based on previous studies, when the length of RVEs is twice larger than the length of the reinforcements, a balance between efficiency and accuracy can be obtained (Zhang et al. 2019b, 2018a). The VF4.5-R RVE contains 425 CNTs, which is very difficult using the manual or original RSA methods.

To characterize the orientation of CNTs in the aligned and random-oriented RVEs. After rigid body dynamics simulation (Fig. 2c), the angles between CNTs and X-axis were calculated and counted. As shown in Fig. 5, for the aligned CNTs (A RVEs), the angles between CNTs and X-axis are mostly less than 12°. In contrast, for the random-oriented CNTs (R RVEs), the angles between CNTs and X-axis have a wide distribution from 0° to 90°. This result proves that the RVEs with random and aligned oriented CNTs

Fig. 3 Flow chart of **a** improved and **b** original RSA method
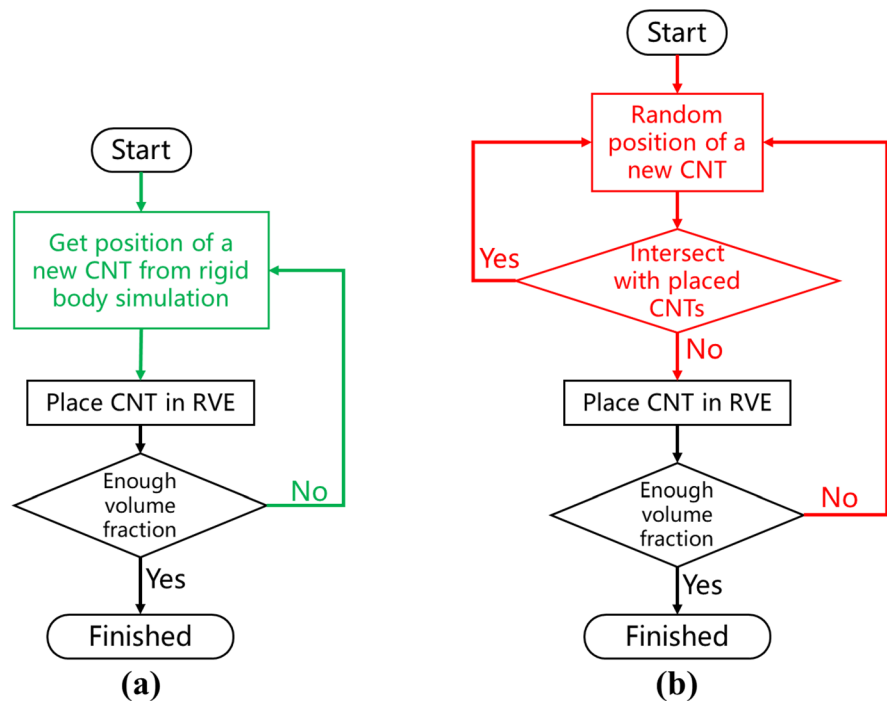
can be obtained efficiently using the enhanced RVE builder.

3 Finite element simulation and results

3.1 Computational homogenization and material properties

The finite element method was used to study the deformation behaviors of CNT/Al. Uniaxial tensile loading was applied to each RVE in Fig. 4. The loadings were along the X-axis and Z-axis, respectively, to analyze the anisotropy of the RVEs. For the aligned RVEs, the X-axis was the longitudinal direction of CNTs; the Z-axis was the transverse direction of CNTs (these simulations were denoted by "T"). More details about the loading conditions can be found in Ref. (Zhang et al. 2018a, 2018b). The stress–strain curves are obtained based on the effective stress σ_{eff} and strain $\varepsilon_{\mathrm{eff}}$ (Zhang et al. 2018b):

$$\sigma_{\mathrm{eff}} = \frac{\sum_1^N f_{\mathrm{rf}}}{A} \tag{11}$$

$$\varepsilon_{\mathrm{eff}} = \frac{U}{L} \times 100\% \tag{12}$$

where A is the area of the loading surface, N is the number of the nodes on that surface, f_{rf} the reaction force at those nodes, U the applied displacement (18 nm in this study, corresponding to the applied strain of 3%), L the side length of the RVEs (600 nm).

To quantitatively characterize the load transfer from Al to CNTs, the average stress in CNTs σ_{cnt} was calculated (Zhang et al. 2018b):

$$\sigma_{\mathrm{cnt}} = \frac{\sum_1^m V_{\mathrm{i}} \sigma_{\mathrm{i}}}{V_{\mathrm{cnt}}} \tag{13}$$

where m is the number of finite elements of CNTs in the finite element model, V_{cnt} the total volume of CNTs, V_{i} and σ_{i} the volume and stress of each element in CNTs, respectively.

Based on Eqs. (11) and (13), the stress concentration factor of CNTs R_{cnt} can be defined (Zhang et al. 2018b):

$$R_{\mathrm{cnt}} = \frac{\sigma_{\mathrm{cnt}}}{\sigma_{\mathrm{eff}}} \tag{14}$$

The stress concentration factor reflects the load transfer efficiency from the matrix to reinforcement.

The Al matrix was modeled by an elastoplastic material law with anisotropic hardening rule, while CNTs were modeled using an ideal elastic material
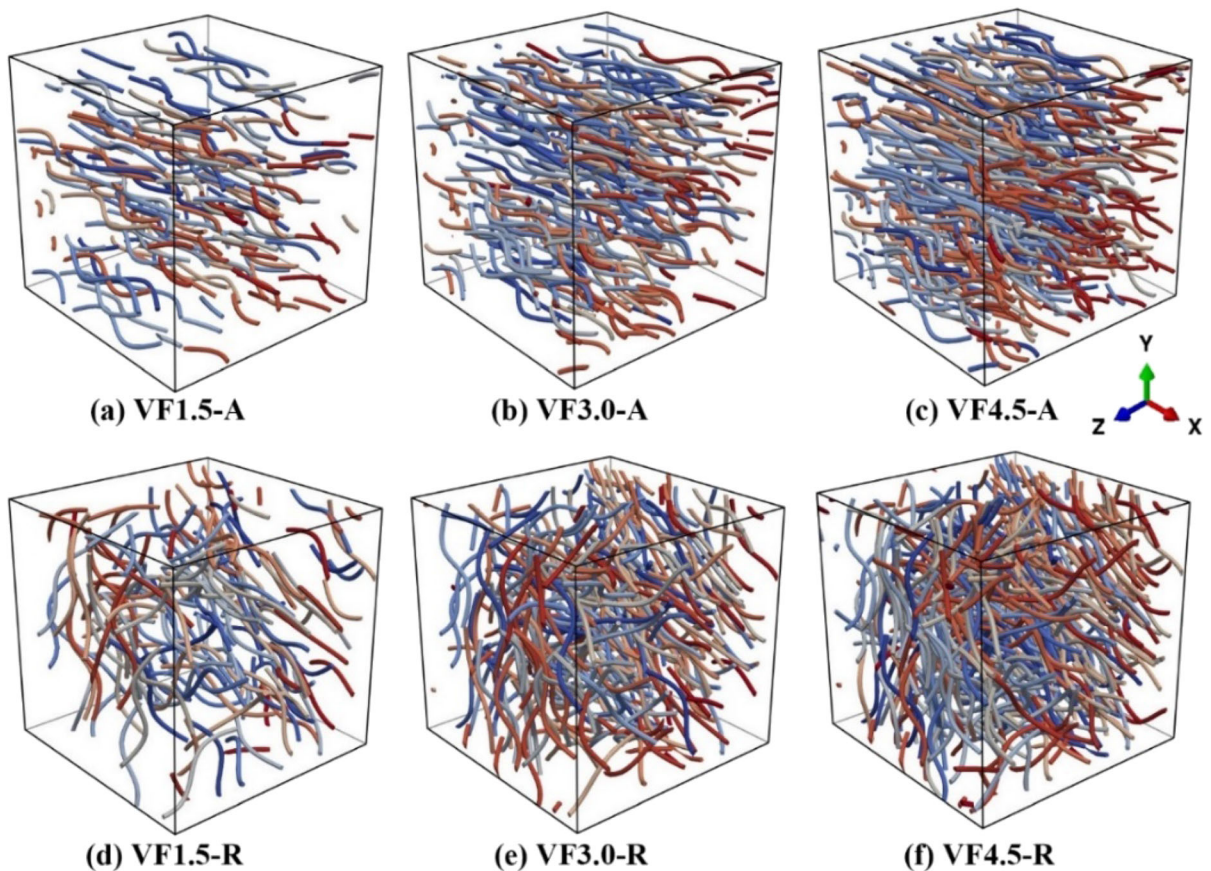
Fig. 4 RVEs of CNT/Al: **a–c** CNTs are aligned along X-axis (denoted by "A"); **d–f** CNTs are randomly oriented (denoted by "R"). Volume fractions of RVEs are **a** and **d** 1.5 vol.%, **b** and **e** 3.0 vol.%, **c** and **f** 4.5 vol.%, respectively

law. The Young's modulus and Poisson's ratio of the Al matrix were 69.5 GPa and 0.33, respectively. The isotropic hardening rule of Al relates the flow stress σ to the equivalent plastic strain ε^p by:

$$\sigma = \sigma_y + K(\varepsilon^p)^n \tag{15}$$

where the yield stress $\sigma_y = 308$ MPa, the hardening parameters $K = 408$ MPa and $n = 0.45$ (Zhang et al. 2020b, 2018a, 2018b). Young's modulus of 750 GPa and Poisson's ratio of 0.2 were used for CNTs (Zhang et al. 2020b).

Because only small deformations were simulated (3% tensile deformation), the damages of the matrix, reinforcement, and interface were not considered in this paper. To simplify the models in this study, the interfaces between CNT and Al of current FE models were set perfectly tied. Still, if needed, three basic interfacial behaviors (adhesion interface, friction interface, and cohesive interface) can be considered (Su et al. 2014; Espinosa et al. 2012).

3.2 Mesh and RVE size

Although smaller mesh sizes and larger RVE sizes provide higher accuracy of the finite element simulations, they require expensive computational costs (Harper et al. 2012; Kanit et al. 2003). To balance the computational cost and simulation accuracy, models with four different mesh sizes and RVE sizes were investigated, as shown in Figs. 6 and 7. The tensile deformations of these models were simulated. The tensile stresses were calculated to determine the relative errors of these models. The relative stress error is defined as:

$$\rho = \left| \frac{\sigma_{\text{eff}} - \sigma_{\text{ref}}}{\sigma_{\text{ref}}} \right| \tag{16}$$
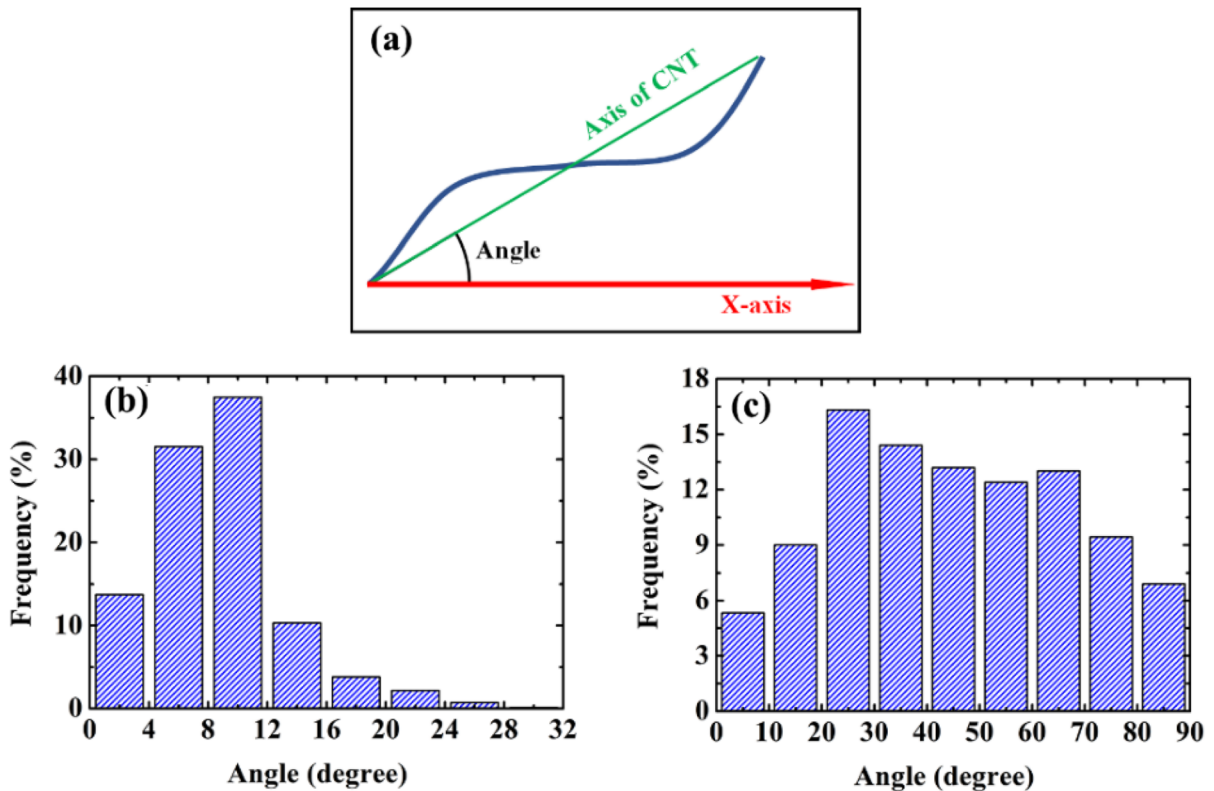
Fig. 5 Frequency of angels between X-axis and CNT axes: **a** diagram of the angle between X-axis and CNT axes, **b** aligned, and **c** random-oriented CNTs

where σ_{eff} is the effective tensile stress, σ_{ref} the reference tensile stress.

As shown in Fig. 6, four models with different mesh sizes were generated. The mesh sizes of the models were controlled by the maximum element volume using Tetgen (Si 2015). The model without maximum element volume constrain was denoted as M-default. Compared to the size of the RVE, the diameters of CNTs are tiny. Therefore, the meshes inside or near CNTs are already very small even without maximum element volume constrain, as shown in Fig. 6a. The models with maximum element volume of 1000 nm^3, 500 nm^3, and 250 nm^3 were denoted as M-1000, M-500, and M-250, respectively. The relative stress errors of M-default, M-500, and M-1000 were calculated and shown in Fig. 6e, while the tensile stresses of M-250 were taken as the reference stresses. From Fig. 6e, with finer mesh sizes, the relative errors are smaller. However, thanks to the tiny diameters of CNTs, even the relative errors

of M-default are less than 2%. Therefore, the default mesh size was used in other simulations in this study.

As shown in Fig. 7, four models with different RVE sizes were generated. The volume fraction of CNT in these models is 1.5 vol.%. All the CNTs are aligned along the X-axis. The edge lengths of L-700, L-600, L-500, and L-400 are 700, 600, 500, and 400 nm, respectively. The model L-600 and VF1.5-A in Fig. 4a are the same RVE model. Taking the tensile stress of L-700 as the reference, the relative errors of other models are shown in Fig. 7e. With larger RVE sizes, the relative errors are smaller. The relative stress errors of L-600 is smaller than 1%. Therefore, the RVEs with an edge length of 600 nm were used in other simulations in this study.

3.3 Calculated stress–strain curves

The stress–strain curves obtained from the simulations are shown in Fig. 8. The flow stress predicted by the aligned RVEs is higher than those from the random

Fig. 6 Models with different mesh sizes. **a** Default mesh size. Models with maximum element volume of **b** 1000 nm³, **c** 500 nm³, and **d** 250 nm³. **e** Relative stress errors

(a) M-default (b) M-1000 (c) M-500
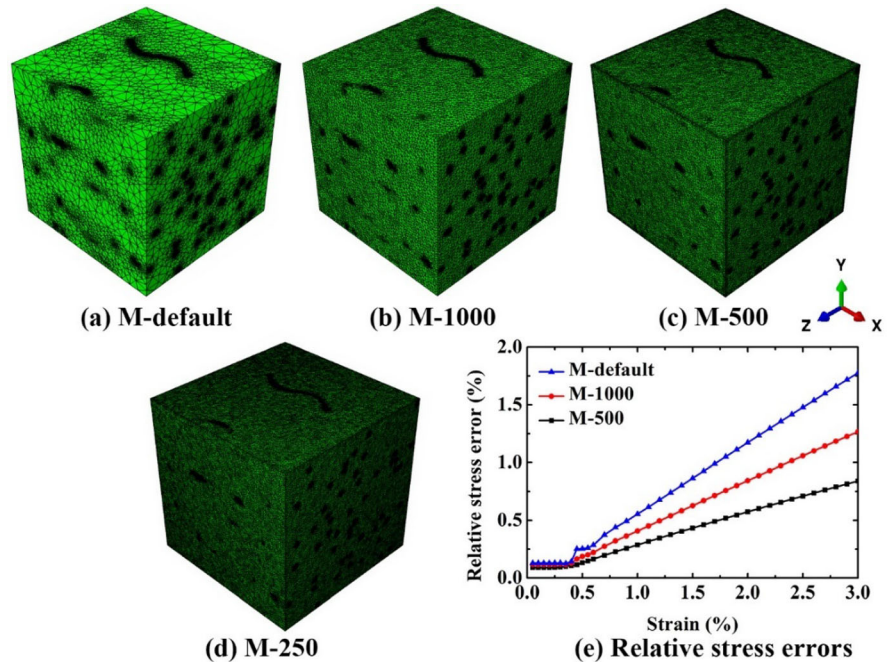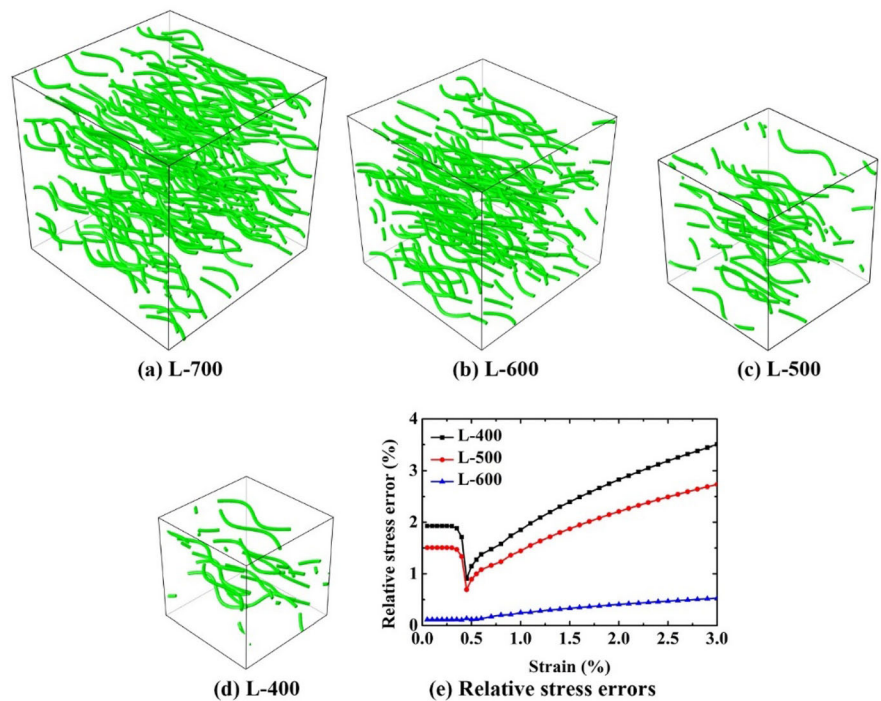
(d) M-250 (e) Relative stress errors

Fig. 7 Models with different RVE sizes. RVE with edge length of **a** 700 nm **b** 600 nm, **c** 500 nm and **d** 400 nm. **e** Relative stress errors

(a) L-700 (b) L-600 (c) L-500

(d) L-400 (e) Relative stress errors

RVEs, even when the volume fractions of random RVEs are higher (Fig. 8a). Figure 8b shows that the yield stresses and flow stresses of different virtual composites are higher than those of pure matrix, as expected. However, the flow stresses predicted by the aligned RVEs with the loading direction along the Y-axis (Fig. 8b) are lower than those predicted by the random RVEs (Fig. 8a) to some degree. These results

confirm that the alignment of CNTs plays a vital role in the load transfer effect.

The effect of the LTSM is investigated by comparing the stress–strain curves of the CNT/Al and pure matrix. The relative increments in the elastic modulus due to the addition of CNTs were calculated and shown in Fig. 9. Figure 9 shows that the predicted increment in elastic modulus matches well with the experimental results (Liu et al. 2013), no matter for aligned (models A and A-T) or random (models R) CNTs.

The metal matrix of the experimental CNT/Al composites in Fig. 9 is 2009Al alloy. However, the matrix of the calculated CNT/Al is pure Al to make the calculated model as simple as possible. Due to alloying and precipitated phases, such as Al_2Cu and Al_2CuMg, the matrix has a higher Young's modulus than pure aluminum. The calculation of Young's modulus of the matrix alloy is another complex problem, which is not the topic of this paper. Therefore, we use the relative increments instead of the exact values of Young's modulus. The exact values of the calculated and experimental Young's moduli are shown in Supplementary file Table.1.

Compared to the unreinforced Al, the 4.5 vol.% CNT/Al with aligned CNTs showed $\sim 28\%$ increment in Young's modulus when the load direction was parallel to the aligned CNTs. When the load was perpendicular to the aligned CNTs or the CNTs were randomly distributed, the 4.5 vol.% CNT/Al only showed $\sim 12\%$ increment in Young's modulus. The prediction accuracy of the RVE based FE models for elastic modulus is verified. However, because other strengthening mechanisms like grain refinement, Orowan looping, and thermal mismatch were not considered here, the predicted strength did not match well with the experimental. These strengthening mechanisms can also be modeled using the finite
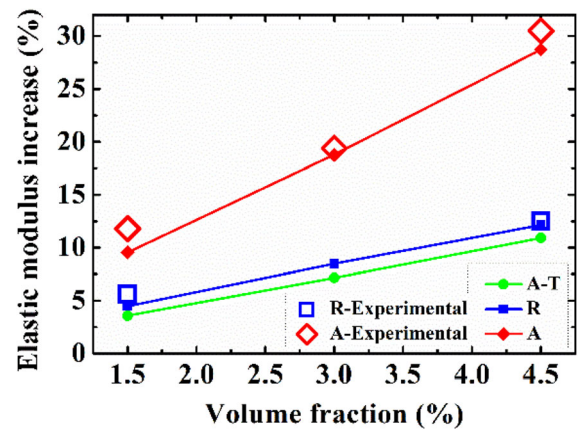

Fig. 9 Relative increments in elastic modulus of CNT/Al. Experimental data of composites with aligned CNTs (A-Experimental) and random CNTs (R-Experimental) were obtained from extruded and friction stir processed CNT/Al (Liu et al. 2013), respectively

element method (Zhang et al. 2019b). However, they are not the topic of this paper. Figure 9 shows that the predicted increments in the elastic modulus by the A-T and R models are close and much smaller than those by the A models.

3.4 Strain and stress of the matrix and reinforcements

Figures 10 and 11 show the equivalent plastic strains of the Al matrix and Mises stress fields of CNTs, respectively, at the applied strain of 0.5%. The 0.5% applied strain is just passed the yield point of the whole composite model according to Fig. 8. At 0.5% applied strain, it is easy to find the serious inhomogeneous deformation caused by the different mechanical properties between CNTs and Al. As shown in Fig. 10, even after the whole composite has passed the yield point, there are still many areas that have not

Fig. 8 Stress–strain curves obtained from tensile simulations of aligned RVEs along **a** X-axis and **b** Y-axis (denoted as "T")
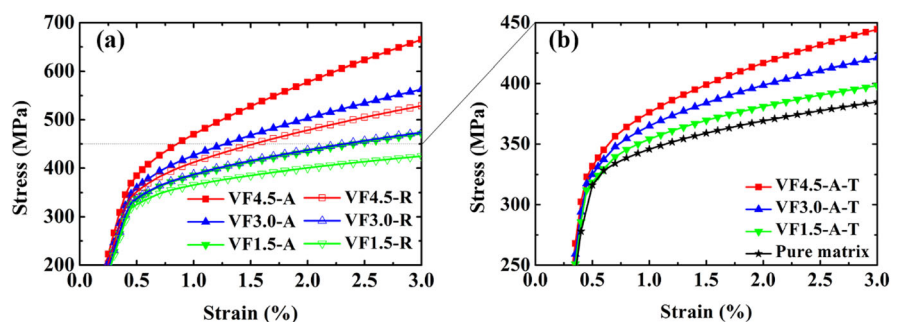
experienced any plastic deformation. The equivalent plastic strains in the Al matrix are affected by the loading direction and volume fraction of CNTs. Generally, with increasing the volume fraction of CNTs, the plastic strain of Al increases. When the loading is parallel to the aligned CNTs (A models), the plastic strain is more inhomogeneous, and the high plastic strain appears near the ends of CNTs. When the loading is perpendicular to the aligned CNTs (A-T models), the plastic strain of Al is more homogeneous, and the high strain appears surrounding CNTs. For the models with randomly distributed CNTs (R models), the plastic strains of Al are also very inhomogeneous.

As shown in Fig. 11, all CNTs bear high stresses for A models, while all CNTs in A-T models bear much lower stresses. For R models, CNTs that are parallel to the loading direction bear high stresses. These results indicate that the load can be transferred to CNTs efficiently only when parallel to the load direction.

3.5 Stress concentration factors

The stress concentration factors were calculated using Eq. (14) and shown in Fig. 12. For all models, R_{cnt} decreases slightly at applied strains of 0.4–0.5% and then increases. This load-rebalance phenomenon was also observed in the previous report (Zhang et al. 2018a). The load-rebalance phenomenon is caused by inhomogeneous plastic deformation of the matrix before the macroscopic yield of CNT/Al (Zhang et al. 2018a). For A models, R_{cnt} decreases with the increase of volume fraction, indicating that a higher volume fraction of CNTs leads to a lower load transfer efficiency. For R and A-T models, the volume fraction of CNTs affects the R_{cnt} slightly.

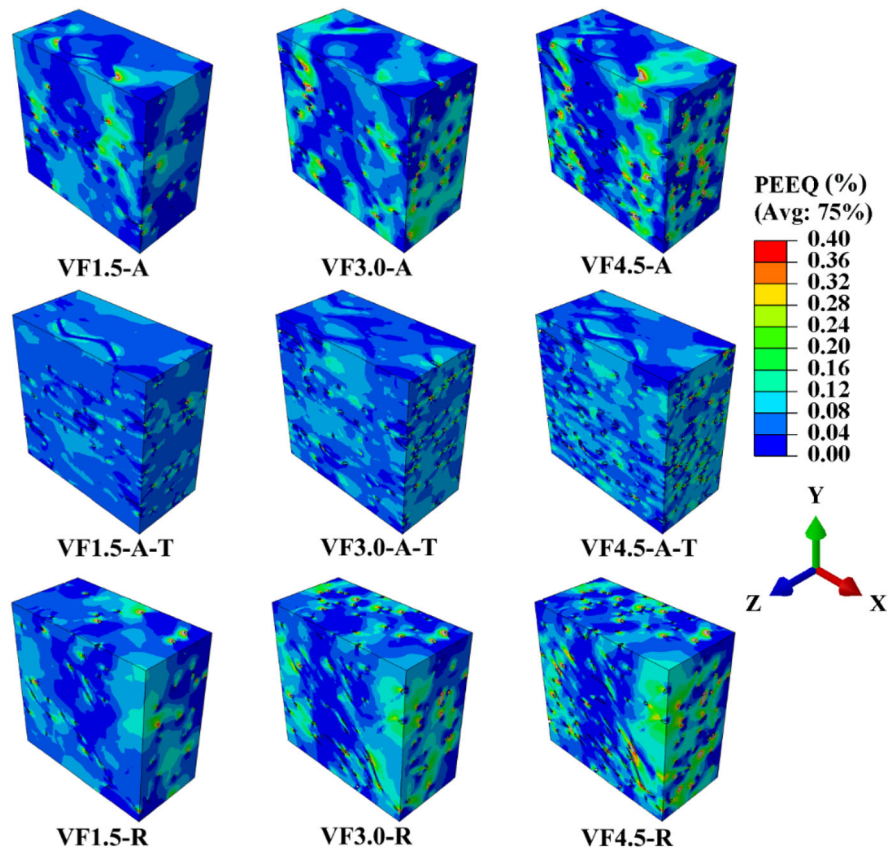**Fig. 10** The equivalent plastic strain field in the Al matrix at an applied strain of 0.5%

Fig. 11 Mises stress fields of CNTs at an applied strain of 0.5%
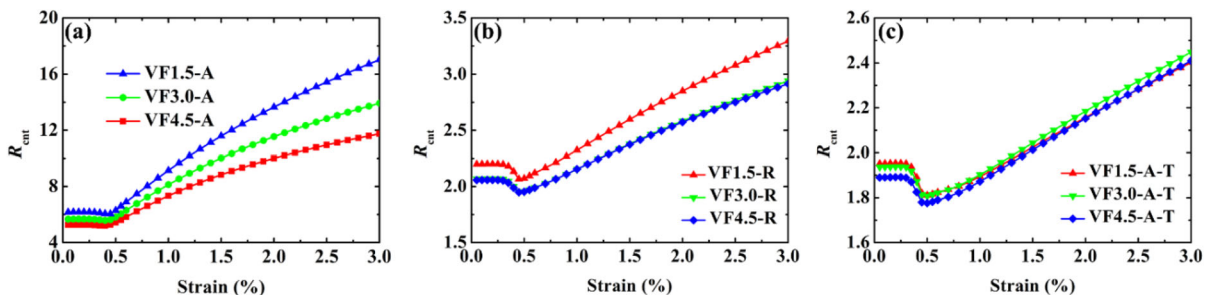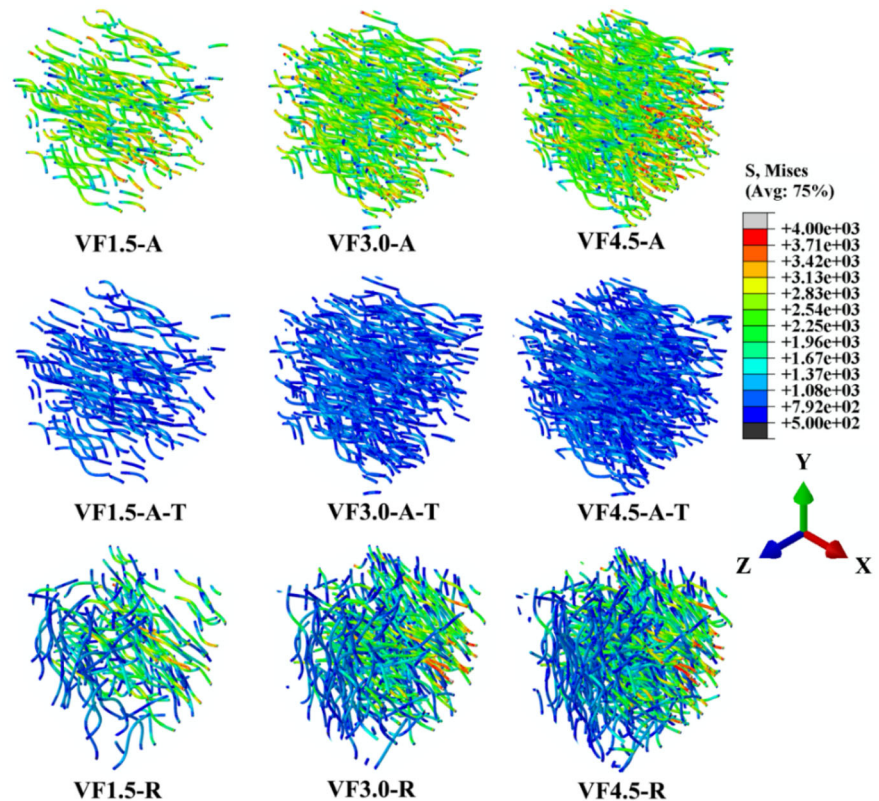

Fig. 12 Evolution of stress concentration factor of CNTs during tensile deformation: **a** aligned CNTs, **b** random CNTs, and **c** aligned CNTs with transverse loading direction

4 Discussion

4.1 More cases of structural models of CNT/Al composites

To demonstrate the flexibility of the proposed RVE builder, two more cases of structural models of CNT/Al composites have been built. In Fig. 13a, two kinds of reinforcements (spheres and straight fibers) were used to model a hybrid reinforced composite. The

spheres can be used to model the CNT clusters (Zhang et al. 2020b). If the spheres in Fig. 13a are removed, a composite model with some CNT-free zones can be obtained, as shown in Fig. 13b. The CNT/Al composites with CNT-free and CNT-rich zones are believed to have enhanced strength-ductility properties (Liu et al. 2020; Huang et al. 2015; Ma et al. 2021a, b, c; Xu et al. 2017, 2018), which is gaining attention in recent years. The proposed RVE builder is capable of building CNT/Al models with CNT-rich and CNT-free zones.

Fig. 13 Models of **a** hybrid reinforced composites and **b** composite with CNT blank areas

(a) Fiber-Sphere   **(b) Spheres removed**
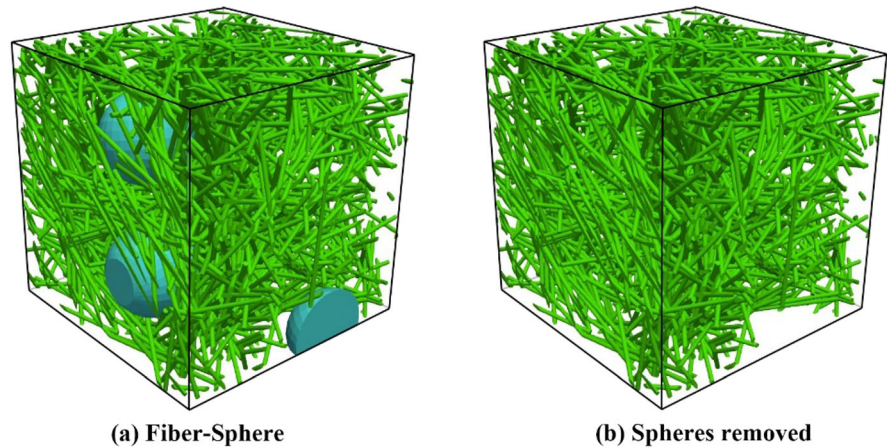
Taking advantage of the enhanced RVE builder, various structural CNT/Al composites can be built. Based on the structural models, the mechanical properties of the composites can be predicted, even if the structures have not been manufactured. Therefore, it is possible to use the enhanced RVE builder to predict the mechanical properties of the new CNT/Al during the design process. However, the prediction of the mechanical properties also needs precise mechanical parameters of CNT(O'Connell 2018), Al matrix(Zhang et al. 2019b; Su et al. 2014), precipitated phases(Ding et al. 2018), CNT clusters (Zhang et al. 2020b), and interfaces (Fan et al. 2018), which is difficult to acquire and not the topic of this study. In summary, the enhanced RVE builder solved the RVE building problems, however, there are still a lot of other problems that need to be solved before an accurate materials design can be concluded.

With a high volume fraction of curved/straight fibers, the RVEs can be used not only to study CNT/Al composites, but also many other materials, such as carbon-fiber-reinforced polymers (Aamir et al. 2019) and SiC fiber-reinforced SiC matrix composite (Wang et al. 2020b).

4.2 Advantages and disadvantages of the proposed RVE builder

Compared to other sedimentation-based algorithms (Staub et al. 2018; Gaiselmann et al. 2013; Feng et al. 2003), controllable volume fraction and fiber orientation are the advantages of the proposed RVE builder. For other sedimentation-based algorithms, the RVE size is related to the compression or sedimentation

process. To get the desired volume fraction, the compression or sedimentation needs to be modified, which may change the RVE shapes. For the proposed RVE builder, the RVE shape and volume fraction is decided by the RVE zone selecting step, which makes it possible to generate desired RVE shape and volume fraction. By adjusting the motion state (activated or deactivated), the orientations of the fibers can be controlled, which is also not supported in other sedimentation-based algorithms.

Compared to the random-walk-based algorithm (Altendorf and Jeulin 2011), the flexibility of reinforcements shapes is the advantage of the proposed RVE builder. For the random-walk-based algorithm, the shapes of the fibers are generated during the "walking", which makes it difficult to control the final shapes.

The maximum volume fraction is the disadvantage of the proposed RVE builder, compared to both random-walk-based algorithms and other sedimentation-based algorithms. The maximum CNTs volume fraction of the proposed RVE builder is still limited. It is influenced by the CNT shape and the desired orientation. For current CNT shapes in Fig. 2a, the maximum volume fraction is around 10% and 18% for randomly and aligned oriented CNTs, respectively. For the random-walk-based algorithm, the maximum volume fraction of the fibers can reach 50% (Altendorf and Jeulin 2011). Because of the orientation control of the fibers in rigid body simulation, the fibers are not compressed to the maximum density, which makes them have less maximum volume fraction than other sedimentation-based algorithms. Even so, the maximum volume fraction is high enough for CNT/Al,

which has less than 10 vol.% CNT normally (Jagan-natham et al. 2020).

5 Conclusions

A rigid body dynamics simulation enhanced RVE builder was developed. A series of 3D RVEs were built, with various alignment and volume fractions of CNTs. Based on these RVEs, finite element models were built to explore the LTSM in CNT/Al. Simulations of tensile deformations were carried out, which predicted Young's moduli, yield stresses, and stress–strain curves of different virtual composites. The following conclusions can be derived:

1. Rigid body dynamics simulation enhanced RVE builder can reduce the 'framing effect' and construct the RVEs of CNT/Al with high volume fractions of CNTs. The new RVE builder is more than 20 times faster than the original RSA method. The volume fraction can be set accurately. Using this new method, the orientation of CNTs in the RVEs can be modified.
2. Higher volume fraction of CNTs leads to higher Young's modulus and yield stress of CNT/Al. The CNT/Al with the aligned CNTs has higher stiffness and strength along the longitudinal direction.
3. The LTSM contributes to the increment in Young's modulus of CNT/Al dominantly.

Declarations

References

Aamir, M., Tolouei-Rad, M., Giasin, K., Nosrati, A.: Recent advances in drilling of carbon fiber–reinforced polymers for aerospace applications. Int. J. Adv. Manuf. Technol. **105**, 2289–2308 (2019)

Altendorf, H., Jeulin, D.: Random-walk-based stochastic modeling of three-dimensional fiber systems. Phys. Rev. E **83**, 041804 (2011)

Azarniya, A., Azarniya, A., Sovizi, S., Hosseini, H.R.M., Varol, T., Kawasaki, A., Ramakrishna, S.: Physicomechanical properties of spark plasma sintered carbon nanotube-reinforced metal matrix nanocomposites. Prog. Mater. Sci. **90**, 276–324 (2017)

B.O. Community: Blender-A 3D modelling and rendering package, Blender Foundation, Stichting Blender Foundation, Amsterdam (2018)

Chen, X., Tao, J., Liu, Y., Bao, R., Li, F., Li, C., Yi, J.: Interface interaction and synergistic strengthening behavior in pure copper matrix composites reinforced with functionalized carbon nanotube-graphene hybrids. Carbon **146**, 736–755 (2019)

Ding, L., Jia, Z., Nie, J.-F., Weng, Y., Cao, L., Chen, H., Wu, X., Liu, Q.: The structural and compositional evolution of precipitates in Al-Mg-Si-Cu alloy. Acta Mater. **145**, 437–450 (2018)

Efimov, A.E., Tonevitsky, A.G., Dittrich, M., Matsko, N.B.: Atomic force microscope (AFM) combined with the ultramicrotome. J. Microsc. **226**, 207–216 (2007)

Ericson, C.: Real-Time Collision Detection. Crc Press, London (2004)

Erwin, C.: Bullet Physics Simulation Introduction to rigid body dynamics and collision detection, (2015)

Espinosa, H.D., Filleter, T., Naraghi, M.: Multiscale experimental mechanics of hierarchical carbon-based materials. Adv. Mater. **24**, 2805–2823 (2012)

Fan, G., Jiang, Y., Tan, Z., Guo, Q., Xiong, D., Su, Y., Lin, R., Hu, L., Li, Z., Zhang, D.: Enhanced interfacial bonding and mechanical properties in CNT/Al composites fabricated by flake powder metallurgy. Carbon **130**, 333–339 (2018)

Feng, Y.T., Han, K., Owen, D.R.J.: Filling domains with disks. Int. J. Numer. Methods Eng. **56**, 699–713 (2003)

Figiel, Ł: Nonlinear multiscale modelling of quasi-solid state behaviour of PET/MWCNT nanocomposites. Compos. Commun. **8**, 101–105 (2018)

Gaiselmann, G., Froning, D., Tötzke, C., Quick, C., Manke, I., Lehnert, W., Schmidt, V.: Stochastic 3D modeling of non-woven materials with wet-proofing agent. Int. J. Hydrog. Energy **38**, 8448–8460 (2013)

Gaiselmann, G., Tötzke, C., Manke, I., Lehnert, W., Schmidt, V.: 3D microstructure modeling of compressed fiber-based materials. J. Power Sources **257**, 52–64 (2014)

Ghossein, E., Lévesque, M.: Random generation of periodic hard ellipsoids based on molecular dynamics. J. Comput. Phys. **253**, 471–490 (2013)

Guven, I., Cinar, K.: Micromechanical modeling of particulate-filled composites using micro-CT to create representative volume elements. Int. J. Mech. Mater. Des. **15**, 695–714 (2019)

Han, K., Feng, Y.T., Owen, D.R.J.: Sphere packing with a geometric based compression algorithm. Powder Technol. **155**, 33–41 (2005)

Harjo, S., Tsuchida, N., Abe, J., Gong, W.: Martensite phase stress and the strengthening mechanism in TRIP steel by neutron diffraction. Sci. Rep. **7**, 15149 (2017)

Harper, L.T., Qian, C., Turner, T.A., Li, S., Warrior, N.A.: Representative volume elements for discontinuous carbon fibre composites–Part 2: determining the critical size. Compos. Sci. Technol. **72**, 204–210 (2012)

Huang, L.J., Geng, L., Peng, H.-X.: Microstructurally inhomogeneous composites. Prog. Mater. Sci. **71**, 93–168 (2015)

Jagannatham, M., Chandran, P., Sankaran, S., Haridoss, P., Nayan, N., Bakshi, S.R.: Tensile properties of carbon nanotubes reinforced aluminum matrix composites. Carbon **160**, 14–44 (2020)

Joshi, U.A., Sharma, S.C., Harsha, S.P.: Characterizing the strength and elasticity deviation in defective CNT reinforced composites. Compos. Commun. **2**, 9–14 (2016)

Kanit, T., Forest, S., Galliet, I., Mounoury, V., Jeulin, D.: Determination of the size of the representative volume element for random composites: statistical and numerical approach. Int. J. Solids Struct. **40**, 3647–3679 (2003)

Kelly, T.F., Miller, M.K.: Atom probe tomography. Rev. Sci. Instrum. **78**, 031101 (2007)

Khalevitsky, Yu.V., Konovalov, A.V.: A gravitational approach to modeling the representative volume geometry of particle-reinforced metal matrix composites. Eng. Comput. **35**, 1037–1044 (2019)

Lam, T.N., Wu, S.C., Chae, H., Chen, S.W., Jain, J., Lee, S.Y., An, K., Vogel, S.C., Chiu, S.M., Yu, D., et al.: Phase stress partition in gray cast iron using in situ neutron diffraction measurements. Metall. Mater. Trans. A **2**, 831 (2020)

Li, X., Yu, B., Wang, P., Zhang, X., Fan, T., Yang, J.: Unit cells for thermal analyses of syntactic foams with imperfect interfaces. Compos. Commun. **3**, 28–32 (2017)

Liu, Z.Y., Xiao, B.L., Wang, W.G., Ma, Z.Y.: Singly dispersed carbon nanotube/aluminum composites fabricated by powder metallurgy combined with friction stir processing. Carbon **50**, 1843–1852 (2012)

Liu, Z.Y., Xiao, B.L., Wang, W.G., Ma, Z.Y.: Developing high-performance aluminum matrix composites with directionally aligned carbon nanotubes by combining friction stir processing and subsequent rolling. Carbon **62**, 35–42 (2013)

Liu, Z.Y., Xiao, B.L., Wang, W.G., Ma, Z.Y.: Effect of carbon nanotube orientation on mechanical properties and thermal expansion coefficient of carbon nanotube-reinforced aluminum matrix composites. Acta Metall. Sin. Engl. Lett. **27**, 901–908 (2014)

Liu, Z.Y., Zhao, K., Xiao, B.L., Wang, W.G., Ma, Z.Y.: Fabrication of CNT/Al composites with low damage to CNTs by a novel solution-assisted wet mixing combined with powder metallurgy processing. Mater. Des. **97**, 424–430 (2016)

Liu, Z.Y., Xiao, B.L., Wang, W.G., Ma, Z.Y.: Modelling of carbon nanotube dispersion and strengthening mechanisms in Al matrix composites prepared by high energy ball milling-powder metallurgy method. Compos. Part Appl. Sci. Manuf. **94**, 189–198 (2017)

Liu, Z.Y., Ma, K., Fan, G.H., Zhao, K., Zhang, J.F., Xiao, B.L., Ma, Z.Y.: Enhancement of the strength-ductility relationship for carbon nanotube/Al–Cu–Mg nanocomposites by material parameter optimisation. Carbon **157**, 602–613 (2020)

Ma, G., Dong, W., Liu, Z., Bi, S., Zan, Y., Xiao, B., Ma, Z.: Effect of hot pressing temperature on microstructure and tensile properties of SiC/Al-Zn-Mg-Cu composites. Acta Metall. Sin. **55**, 1319–1328 (2019)

Ma, K., Liu, Z.Y., Bi, S., Zhang, X.X., Xiao, B.L., Ma, Z.Y.: Microstructure evolution and hot deformation behavior of carbon nanotube reinforced 2009Al composite with bimodal grain structure. J. Mater. Sci. Technol. **70**, 73–82 (2021a)

Ma, K., Li, X.N., Liu, K., Chen, X.G., Liu, Z.Y., Xiao, B.L., Ma, Z.Y.: Improving the high-cycle fatigue strength of heterogeneous carbon nanotube/Al-Cu-Mg composites through grain size design in ductile-zones. Compos. Part B Eng. **222**, 109094 (2021)

Ma, K., Liu, Z.Y., Liu, K., Chen, X.G., Xiao, B.L., Ma, Z.Y.: Structure optimization for improving the strength and ductility of heterogeneous carbon nanotube/Al–Cu–Mg composites. Carbon **178**, 190–201 (2021c)

Mokdad, F., Chen, D.L., Liu, Z.Y., Xiao, B.L., Ni, D.R., Ma, Z.Y.: Deformation and strengthening mechanisms of a carbon nanotube reinforced aluminum composite. Carbon **104**, 64–77 (2016)

Müller, V., Kabel, M., Andrä, H., Böhlke, T.: Homogenization of linear elastic properties of short-fiber reinforced composites–a comparison of mean field and voxel-based methods. Int. J. Solids Struct. **67–68**, 56–70 (2015)

O'Connell, M.J.: Carbon Nanotubes: Properties and Applications. CRC Press, London (2018)

Pérez, L., Cabrera, I., Santiago, A.A., Vargas, J., Beltrán, A., Alfonso, I.: Effect of the Al–CNT interlayer on the tensile elastic modulus of Al matrix composites with random dispersion of CNTs. J. Braz. Soc. Mech. Sci. Eng. **40**, 550 (2018)

Redenbach, C., Shklyar, I., Andrä, H.: Laguerre tessellations for elastic stiffness simulations of closed foams with strongly varying cell sizes. Int. J. Eng. Sci. **50**, 70–78 (2012)

Roy, S., Gibmeier, J., Schell, K.G., Bucharsky, E.C., Weidenmann, K.A., Wanner, A., Hoffmann, M.J.: Internal load transfer in an interpenetrating metal/ceramic composite material studied using energy dispersive synchrotron X-ray diffraction. Mater. Sci. Eng. A **753**, 247–252 (2019)

Salnikov, V., Choï, D., Karamian-Surville, P.: On efficient and reliable stochastic generation of RVEs for analysis of composites within the framework of homogenization. Comput. Mech. **55**, 127–144 (2015)

Schroeder, W.J., Lorensen, B., Martin, K.: The visualization toolkit: an object-oriented approach to 3D graphics, the visualization toolkit: an object-oriented approach to 3D graphics. Kitware **2**, 109 (2004)

Sheng, P., Zhang, J., Ji, Z.: An advanced 3D modeling method for concrete-like particle-reinforced composites with high volume fraction of randomly distributed particles. Compos. Sci. Technol. **134**, 26–35 (2016)

Sheng, P., Chen, Z., Zhang, J., Ji, Z.: Evolution and heredity of particle distribution in the free-fall method of modeling

particle-reinforced concrete-like composites. Powder Technol. **353**, 1–9 (2019)

Si, H.: TetGen, a delaunay-based quality tetrahedral mesh generator. ACM Trans. Math. Softw. **41**, 1–36 (2015)

Staub, S., Andrä, H., Kabel, M.: Fast FFT based solver for rate-dependent deformations of composites and nonwovens. Int. J. Solids Struct. **154**, 33–42 (2018)

Su, Y., Li, Z., Jiang, L., Gong, X., Fan, G., Zhang, D.: Computational structural modeling and mechanical behavior of carbon nanotube reinforced aluminum matrix composites. Mater. Sci. Eng. A **614**, 273–283 (2014)

Suárez, S., Ramos-Moore, E., Mücklich, F.: A high temperature X-ray diffraction study of the influence of MWCNTs on the thermal expansion of MWCNT/Ni composites. Carbon **51**, 404–409 (2013)

Wang, Z., Yuan, Y.: Micromechanics-based modeling of elastic modulus and coefficient of thermal expansion for CNT-metal nanocomposites. Int. J. Mech. Mater. Des. **16**, 783–799 (2020)

Wang, Z., Yang, F., Shang, J., Wei, N., Kou, L., Li, C.: Mechanical properties of CNT-reinforced Ni3Al composites. J. Phys. Condens. Matter **32**, 205301 (2020)

Wang, J., Chen, Y., Feng, Y., Zhao, G., Jian, X., Huang, Q., Yang, L., Xu, J.: Influence of porosity on anisotropic thermal conductivity of SiC fiber reinforced SiC matrix composite. Ceram. Int. **46**, 28693–28700 (2020b)

Xie, Y., Meng, X., Huang, Y., Li, J., Cao, J.: Deformation-driven metallurgy of graphene nanoplatelets reinforced aluminum composite for the balance between strength and ductility. Compos. Part B Eng. **177**, 107413 (2019)

Xu, R., Tan, Z., Xiong, D., Fan, G., Guo, Q., Zhang, J., Su, Y., Li, Z., Zhang, D.: Balanced strength and ductility in CNT/Al composites achieved by flake powder metallurgy via shift-speed ball milling. Compos. Part Appl. Sci. Manuf. **96**, 57–66 (2017)

Xu, R., Tan, Z., Fan, G., Ji, G., Xiong, D.-B., Guo, Q., Su, Y., Li, Z., Zhang, D.: High-strength CNT/Al-Zn-Mg-Cu composites with improved ductility achieved by flake powder metallurgy via elemental alloying. Compos. Part Appl. Sci. Manuf. **111**, 1–11 (2018)

Xu, R., Tan, Z., Fan, G., Ji, G., Li, Z., Guo, Q., Li, Z., Zhang, D.: Microstructure-based modeling on structure-mechanical property relationships in carbon nanotube/aluminum composites. Int. J. Plast. **120**, 278–295 (2019)

Ye, T., Xu, Y., Ren, J.: Effects of SiC particle size on mechanical properties of SiC particle reinforced aluminum metal matrix composite. Mater. Sci. Eng. A **753**, 146–155 (2019)

Yu, Y., Cui, J., Han, F.: An effective computer generation method for the composites with random distribution of large numbers of heterogeneous grains. Compos. Sci. Technol. **68**, 2543–2550 (2008)

Zhang, X.X., Xiao, B.L., Andra, H., Ma, Z.Y.: Homogenization of the average thermo-elastoplastic properties of particle reinforced metal matrix composites: the minimum representative volume element size. Compos. Struct. **113**, 459–468 (2014a)

Zhang, X.X., Zhang, Q., Zangmeister, T., Xiao, B.L., Andrä, H., Ma, Z.Y.: A three-dimensional realistic microstructure model of particle-reinforced metal matrix composites. Model. Simul. Mater. Sci. Eng. **22**, 035010 (2014)

Zhang, J.F., Zhang, X.X., Wang, Q.Z., Xiao, B.L., Ma, Z.Y.: Simulation of anisotropic load transfer and stress distribution in SiCp/Al composites subjected to tensile loading. Mech. Mater. **122**, 96–103 (2018a)

Zhang, J.F., Zhang, X.X., Wang, Q.Z., Xiao, B.L., Ma, Z.Y.: Simulations of deformation and damage processes of SiCp/Al composites during tension. J. Mater. Sci. Technol. **34**, 627–634 (2018b)

Zhang, X., Zheng, Z., Gao, Y., Geng, L.: Progress in high throughput fabrication and characterization of metal matrix composites. Acta Metall. Sin. **55**, 109–125 (2019a)

Zhang, J.F., Andrä, H., Zhang, X.X., Wang, Q.Z., Xiao, B.L., Ma, Z.Y.: An enhanced finite element model considering multi strengthening and damage mechanisms in particle reinforced metal matrix composites. Compos. Struct. **226**, 111281 (2019)

Zhang, J.Y., Chen, T.J., Zhang, X.Z., Gao, M., Geng, L.B.: Simultaneously strengthening and toughening a core-shell structured particulate reinforced aluminum alloy-based composite by solid solution treatment. J. Alloys Compd. **842**, 155765 (2020)

Zhang, X.X., Zhang, J.F., Liu, Z.Y., Gan, W.M., Hofmann, M., Andrä, H., Xiao, B.L., Ma, Z.Y.: Microscopic stresses in carbon nanotube reinforced aluminum matrix composites determined by in-situ neutron diffraction. J. Mater. Sci. Technol. **54**, 58–68 (2020b)

Zhao, K., Liu, Z., Xiao, B., Ma, Z.: Friction stir welding of carbon nanotubes reinforced Al-Cu-Mg alloy composite plates. J. Mater. Sci. Technol. **33**, 1004–1008 (2017)

Zhao, K., Liu, Z.Y., Xiao, B.L., Ni, D.R., Ma, Z.Y.: Origin of insignificant strengthening effect of CNTs in T6-treated CNT/6061Al composites. Acta Metall. Sin. Engl. Lett. **31**, 134–142 (2018)

Zhou, B., Wang, L., Zhu, G., Wang, J., Wen, W., Zeng, X.: Understanding the strengthening effect of β1 precipitates in Mg-Nd using in situ synchrotron X-ray diffraction. JOM **70**, 2315–2320 (2018)

Zhou, Q.: PyMesh—Geometry Processing Library for Python, Software available for download at https://github.com/PyMesh/PyMesh (2020)

Zhu, X., Zhao, Y., Ma, L., Zhang, G., Ren, W., Peng, X., Hu, N., Rintoul, L., Bell, J.M., Yan, C.: Graphene coating makes copper more resistant to plastic deformation. Compos. Commun. **12**, 106–111 (2019)